RSC Advances

PAPER

View Article Online
View Journal | View Issue

Cite this: *RSC Adv.*, 2020, **10**, 41110

Development of micropillar array electrodes for highly sensitive detection of biomarkers†

Chaozhan Chen,[a] Bin Ran,[a] Zhenxing Wang,[b] Hongli Zhao,[b] Minbo Lan,[b] Huaying Chen *[c] and Yonggang Zhu *[c]

Micropillar array electrodes (μAEs) have been widely applied in electrochemical detection owing to their advantages of increased mass transport, lower detection limit, and potential to be miniaturized. This paper reports the fabrication, simulation, surface modification, and characterization of PDMS-based μAEs coated with gold films. The μAEs consist of 9 × 10 micropillars with a height of either 100 μm, 300 μm, or 500 μm in a 0.09 cm^2 region. Numerical simulation was employed to study the influence of geometrical parameters on the current density. The μAEs were fabricated by soft lithography and characterized using both SEM and cyclic voltammetry. Experiments revealed that high pillars enabled enhanced voltammetric current density regardless of the scan rates. The platinum–palladium/multi-walled carbon nanotubes (Pt–Pd/MWCNTs) were coated on the μAEs to improve their electrochemical detection capability. The μAEs demonstrated 1.5 times larger sensitivity compared with the planar electrode when hydrogen peroxide was detected. Furthermore, μAE500 with Pt–Pd/MWCNTs was employed to detect sarcosine, a potential biomarker for prostate cancer. The linear range and limit of detection for sarcosine were from 5 to 60 μM and 1.28 μM, respectively. This detection range covers the concentration of sarcosine in human tissues (0–60 μM). These results suggest that the μAEs have better detection performance in comparison to planar electrodes due to their large surface area and pillar height. This paper provides essential guidelines for the application of μAEs in high sensitivity electrochemical detection of low abundance analytes.

Received 8th September 2020
Accepted 23rd October 2020

DOI: 10.1039/d0ra07694e

rsc.li/rsc-advances

Introduction

The detection and identification of biomarkers are important in biological studies and disease diagnosis such as cancers.[1] In the past few decades, a variety of analytical techniques,[2,3] including immunoassay,[4] electrochemistry,[5] and electrochemiluminescence,[6] have been developed for the detection of disease biomarkers. The electrochemical technique is one of the most attractive ways owing to its simplicity, portability, and high sensitivity.[7] Among electrochemical sensors, the amperometric one is reliable and cost-effective and therefore has been broadly implemented to detect a variety of biomarkers,[8] such as glucose,[9] sarcosine[10] and cholesterol.[11]

Compared to the reference and counter electrodes, the working electrode is the most crucial element of the electrochemical sensors and has been attracting plenty of research interest to either increase the sensitivity[12] or reduce the detection limits.[13] According to the geometry, electrodes can be divided into planar and 3D ones. The former ones are the most widely employed electrodes since they are not only cost-effective but easy to fabricate. For example, glassy carbon electrodes, screen-printed electrodes,[14] and conductive films patterned on the substrate[15,16] have been developed. In addition to the planar electrodes, the micropillar array electrodes (μAEs) have attracted research attention as an emerging technology with a better electrical signal due to the increased surface area. The μAEs have been used to detect phenol,[17] biofilm,[18] bone metabolic marker proteins,[19] and metal ions.[20] Compared with the planar electrodes, μAEs significantly enhance the response current and hence provide high sensitivity and low detection limit.[20]

The μAEs are mainly manufactured by complicated techniques involving the LIGA-like process,[17–19] carbonizing the photoresist patterned on a substrate,[21] and homoepitaxially growing.[20] Prehn *et al.* have reported μAEs with 10 μm high pillars fabricated using the photolithography, metallization, and electrodeposition.[22] Sanchez-Molas *et al.* used sputtering

[a]*School of Science, Harbin Institute of Technology, Shenzhen, Shenzhen, 518055, China*

[b]*Shanghai Key Laboratory of Functional Materials Chemistry, School of Chemistry and Molecular Engineering, East China University of Science and Technology, Shanghai, 200237, PR China*

[c]*School of Mechanical Engineering and Automation, Harbin Institute of Technology, Shenzhen, Shenzhen, 518055, China. E-mail: zhuyonggang@hit.edu.cn; chenhuaying@hit.edu.cn*

† Electronic supplementary information (ESI) available. See DOI: 10.1039/d0ra07694e

and deep reactive ion etching (DRIE) to prepare the μAEs with higher micropillar (up to 125 μm),[23] and this approach showed better definition and reproducibility. The μAEs with high micropillar are attractive in electrochemical applications owing to the larger electrode surface areas. The above studies have successfully demonstrated both the manufacture and the capability of μAEs. However, the fabrication processes are generally not only expensive but time-consuming. Additionally, both the aspect ratio and pillar height are limited by the lithography process.[23] Therefore, the facile preparation of the μAEs with the higher micropillar even 3D profile is of critical significance for the development of low-cost and high-sensitivity microsensors for chemical and biological substances.

The effect of the dimension (*e.g.*, diameter, height, and space) of micropillar array electrodes on the voltammetric response has been studied both numerically[24] and experimentally.[22,23] The voltammetric response of μAEs was related to both the height and the density of micropillar. Sánchez-Molas *et al.* studied the effect both parameters on the current density under different scan rates (0.005–0.2 V s^{-1}).[23] They reported that the μAEs with either taller pillars or higher density acquired larger currents.[23] Further, Prehn *et al.* reported the increased pillar height narrowed the potential peak-to-peak separation due to the rapid electrolysis of the material around the cylinder walls.[22]

The above research illustrated the importance of the dimension of μAEs. Therefore, understanding the response current of μAEs under various geometrical parameters is essential to obtain a larger current density. Additionally, for high-density micropillar array, the response current was found to be proportional to the surface area at fast scan rates.[22] However, at low scan rates, there was no significant difference in the response current between the μAEs with low pillars and planar electrodes with the same projection area.[22] Since low scan rates are frequently applied in electrochemical detection of low-concentration analytes, developing μAEs with large response current at low scan rates will benefit their application in electrochemical detection.

Herein, we report the manufacture, simulation, and systematic characterization of micropillar array electrodes to enhance the detection sensitivity. The μAEs was manufactured by sputtering gold on PDMS-based micropillars molded from a 3D-printed master. The platinum-palladium/multi-walled carbon nanotubes (Pt–Pd/MWCNTs) were used to modify the μAEs by simple drop-cast. The electrochemical performance was demonstrated using hydrogen peroxide and sarcosine. The μAEs with high micropillars enabled a larger surface area and current density at low to high scan rates (0.025–1 V s^{-1}). The sensitivity of μAEs toward hydrogen peroxide was higher than that of the planar electrode. The linear detection range and LOD of μAEs for sarcosine were 5–60 μM and 17.1 μA mM^{-1} cm^{-2}, respectively. The paper provided essential guidance for the design and application of μAEs in biomarker detection with high sensitivity.

Experimental

Chemicals

The polydimethylsiloxane (PDMS, Sylgard 184) base and curing agent were purchased from Suzhou Research Materials Microtech Co., Ltd. The phosphate buffer solution (PBS, 0.1 M, pH 7.4), 1*H*,1*H*,2*H*,2*H*-perfluorooctyltrichlorosilane, hydrogen peroxide (H_2O_2), (3-mercaptopropyl)trimethoxysilane (MPTMS), potassium ferrocyanide and potassium ferricyanide were purchased from Shanghai Macklin Biochemical Co., Ltd. The multi-walled carbon nanotubes (MWCNTs, 10–20 nm in diameter, 0.5–2 μm in length, 95%) were bought from Nanjing XFNANO Materials Tech Co. Potassium chloroplatinate (K_2PtCl_6), ethyl acetate, sodium tetrachloropalladate (Na_2PdCl_4), sodium citrate and ethylene glycol (EG) were obtained from Aladdin Industrial Corporation. The Nafion™ 117 solution (5% in a mixture of lower aliphatic alcohols and water) was purchased from Sigma-Aldrich. All chemicals were analytical grade and used without further purifications.

Instrumentation and measurements

The scanning electron microscopic (SEM) and transmission electron microscopic (TEM) images were captured using a ZEISS SUPRA 55 electron microscope (Carl Zeiss, Germany) and a Tecnai G2 spirit TEM (FEI, USA), respectively. The X-ray photoelectron spectroscopy (XPS) analysis was performed on an X-ray photoelectron spectrometer (PHI5000 Versaprobe II, PHI, Japan). The NanoArch P140 (BMF Precision, Shenzhen, China) was employed to print the polymer masters of micropillar arrays. The oxygen plasma treatment and sputtering were carried out using PDC-002 (Harrick, Japan) and PD-400 (Pudivaccum, China), respectively. The electrochemical measurements (*e.g.* cyclic voltammetry and chronoamperometry) were performed using an electrochemical workstation (CHI 660E, Shanghai Chen Hua Instrument Co. Ltd). All experiments were carried out using three electrodes: working, counter, and reference electrodes. The counter electrode was a platinum wire electrode (0.5 mm in diameter, 63 mm in length), and the reference electrode was Ag/AgCl (3.0 M KCl) electrode (Ag/AgCl wire, 0.5 mm in diameter, 45 mm in length).

Numerical simulation

A 3D symmetrical model of the pillar and a diffusion domain (Fig. S1†) were generated in COMSOL to simulate the voltammetric response of μAEs with various dimensions. The center-to-center distance between two adjacent micropillars and the height of the diffusion domain varied from 10 μm to 800 μm and 600 μm to 1600 μm, respectively. The radius of the cylindrical diffusion domain was equal to the half of the center-to-center distance between two adjacent micropillars. The pillar height ranged from 100 μm to 1000 μm. While the scan rate was 100 mV s^{-1} and the height of the diffusion domain was $6\sqrt{(Dt)}$ higher than the pillar, where D was the diffusion coefficient of the oxidized species and t (16 seconds) was the total time for the CV scan.

The diffusional transport of the whole domain was obtained by integration in the radial and axial directions of the domain. The boundary conditions used in the simulations were listed in Table S1.† The diffusional current in a one-electron, fully reversible electrochemical system can be described by:

$$I = 2\pi FD\int_0^{r_{\text{pillar}}}\left(\frac{\partial A}{\partial z}\right)_{z=z_{\text{pillar}}} r\mathrm{d}r + \int_0^{z_{\text{pillar}}}\left(\frac{\partial A}{\partial r}\right)_{r=r_{\text{pillar}}}\mathrm{d}z + \int_{r_{\text{pillar}}}^{r_{\text{domain}}}\left(\frac{\partial A}{\partial z}\right)_{z=0} r\mathrm{d}r,$$

where $A = 5$ mM is the concentration of the oxidized species;[25] F is the Faraday constant; z is the component along the axis of the micropillar; r is the component along the radial direction of the micropillar; r_{pillar} and z_{pillar} are the cylinder radius and height; and r_{domian} is the radius of the diffusion domain. Since this study only analyzed the data with forwarding scan peak, to simplify the simulation process, it is assumed that both the reduced and the oxidized species have the same diffusion coefficient (6.39×10^{-6} cm^2 s^{-1}).[26]

The grid impedance test was performed to determine the optimal mesh size for acquiring accurate results. Additionally, validation was carried out using a model with the geometry reported in a previous study[22] and boundary conditions which were exactly the same as those employed in this study (Fig. S2†). The difference in the current density between simulations in this study and the previous study[22] was less than 3%.

Fabrication of micropillar array electrode

Three types of micropillar array electrodes (see Table S2†) containing 9×10 truncated cones were designed in a 0.09 cm^2 region (Fig. 1). The radii of the top and bottom plane of the cones were 50 μm and 100 μm, respectively. The separation of the cone was 100 μm. The height of the pillars was either 100 μm (μAE100), 300 μm (μAE100) or 500 μm (μAE100).

The UV curable polymer was printed on a glass slide using a 3D printer (NanoArch P140) to form the positive masters (see Fig. 1A(a)) of micropillar array. The PDMS-based micropillar arrays were then manufactured by soft lithography as described elsewhere.[27–30] Briefly, the 3D-printed master was firstly coated with 1*H*,1*H*,2*H*,2*H*-perfluorooctyltrichlorosilane in a vacuum desiccator. Then the PDMS mixture with the volume ratio of 10 (base) : 1(curing agent) was cast against the master and degassed for 30 minutes. After baked at 60 °C overnight, the negative PDMS replicas of micropillar arrays were peeled off from the master (Fig. 1A(b)). The negative PDMS replicas were employed as masters to mass-produce the PDMS micropillar arrays using the aforementioned soft lithography technique (Fig. 1A(c) and (d)).

The PDMS micropillar arrays were sputtered with gold to form conduction layers.[31,32] Briefly, the arrays were oxidized for 30 seconds using an oxygen plasma to form hydroxyl groups.[33,34] Afterward, the arrays were placed in a vacuum desiccator with (3-mercaptopropyl) trimethoxysilane for 20 minutes to obtain the thiol groups (–SH). The arrays were then covered using a steel mask (with a 3 mm × 3 mm window) and placed in a sputter with the power of 300 W, the Ar flow rate of 50–80 sccm and the pressure of 0.2–0.5 Pa to deposit a gold membrane with a thickness of approximately 250 nm on the pillar arrays. The micropillar arrays with the gold film were referred to as μAEs without stated otherwise (Fig. 1A(e)).

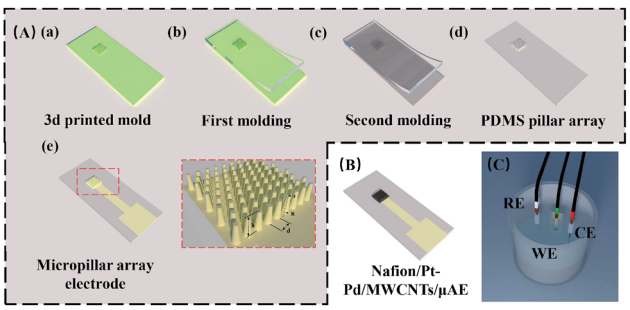

Fig. 1 (A) The schematic diagram showing the fabrication process of the micropillar array electrode using double soft lithography. (a) The positive master from 3D printing of UV curable polymer. (b) The negative mould of the μAE after the first soft lithography. (c) The second soft lithography and (d) the PDMS-based μAE. (e) The PDMS-based μAE sputtered with a gold film. (B) The μAE coated with Nafion/Pt–Pd/MWCNTs. (C) A typical setup of electrochemical detection using a three-electrode sensor.

Synthesis of Pt–Pd/MWCNTs

The Pt–Pd/MWCNTs nanocomposites were synthesized according to the protocols reported in the literature.[35] Briefly, MWCNTs were immersed in the mixture of concentrated HNO_3 and H_2SO_4 (v/v, 1 : 3) at 80 °C for 8 hours to improve the water solubility. Then, 10 mg MWCNTs were dispersed in 10 mL EG solutions (50% in water) with 30 minute ultrasonication. The MWCNTs suspension was added to an EG solution (30 mL, 50% in water) containing 24.3 mg K_2PtCl_6 (50 μmol), 14.7 mg Na_2PdCl_4 (50 μmol) and 10 mg trisodium citrate. The pH value of the solution was then adjusted to 10 using NaOH. The mixture solution was deoxygenated by nitrogen for 30 minutes and then incubated at 100 °C for eight hours with continuous stirring. Finally, the reaction products (Pt–Pd/MWCNTs) were filtrated, washed, and vacuum-dried at 50 °C overnight.

Modification of the micropillar array electrodes

The μAEs were modified to promote analytical performance further. One μL Pt–Pd/MWCNTs suspension was pipetted onto the surface of the μAEs and dried at room temperature. Subsequently, four μL Nafion (0.05 wt%) was added to the same region of the μAEs and dried at room temperature, before stored at 4 °C in the phosphate buffer solution (PBS) for the following electrochemical detection. The μAEs coated with nanomaterials were referred to as Nafion/Pt–Pd/MWCNTs/μAE in this paper (Fig. 1B).

Manufacture of sarcosine biosensors

The μAE500-Nafion/Pt–Pd/MWCNTs was employed to detect sarcosine. Four μL sarcosine oxidase solution (1 kU mL^{-1}) was added to the surface of the electrodes and dried at 4 °C. The electrodes were further coated with four μL Nafion solution

(0.05 wt%) and dried at room temperature. The biosensors were finally washed with phosphate buffer (0.1 M, pH 7.4) and stored at 4 °C for further usage.

Cyclic voltammetry and chronoamperometry measurements

The working, reference, and counter electrodes were directly immersed into a small vial containing the analyte solution to perform electrochemical detection (Fig. 1C). The electrochemically active area of the μAEs was studied using cyclic voltammetry in 5.0 mM $K_3[Fe(CN)_6]/K_4[Fe(CN)_6]$ solution containing 0.5 M KCl. As a benchmark, a planar electrode with the same projected area was tested to demonstrate the performance of the μAEs. The hydrogen peroxide and sarcosine were detected using chronoamperometry at a potential of +600 mV for 90 seconds. The current responses were recorded after 80 seconds when the current was steady. All experiments were repeated at least three times.

Results and discussion

Numerical evaluation of micropillar array electrodes

The μAEs were developed to obtain the increased electrical signal since they possess the much larger surface area than the planar electrodes with the same projected area (A_{pa}). The dimension (*e.g.*, diameter, height, and separation) of the μAEs significantly influenced their surface area. To this end, understanding the influence of geometrical parameters of the μAEs on the response current is of critical importance for the development of electrochemical biosensors based on μAEs.

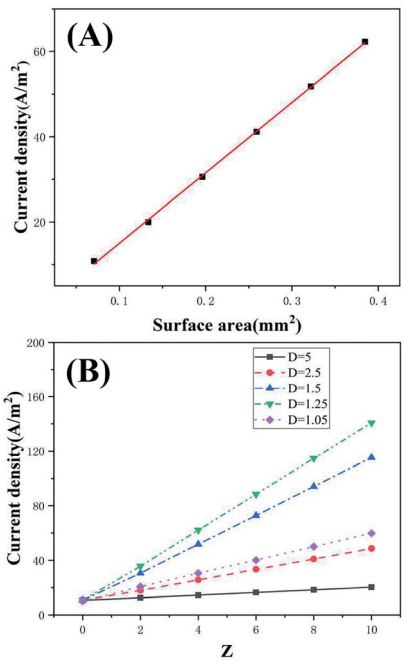

Fig. 2 (A) Variation of current density of the μAEs with surface area when the pillar height varied from 100 to 500 μm. (B) Current density of the μAEs as a function of normalized height (Z) at different separations (D).

The numerical simulation was employed to study the impact of surface area (caused by varying pillar height) as well as the height and separation normalized to the bottom radius of pillars. As shown in Fig. S3,† the current density becomes larger as pillar height increased. The increase of the pillar height directly results in an increase of the electrode surface area. Fig. 2A clearly depicts that the current density, *i.e.*, the ratio between the anodic peak current (i_{pc}) and the projection area, is directly proportional to the surface area (S) of the μAEs. The relationship can be described by a linear model of: i_{pc}/A_{pa} (A m^{-2}) = 165.1S (mm^2)–1.52 (R^2 = 0.99). This linear relationship suggests the planar diffusion dominates the response of the μAEs which is in agreement with the findings by Sánchez-Molas.[23] Additionally, the current density of μAEs with the height of 100, 300, and 500 μm is 0.85, 2.83, and 4.8 times larger than that of the planar electrode, respectively. Therefore, μAEs with a large surface area can be used to obtain electrical signals with increased intensities.

The influence of the dimension, *e.g.*, radius, height, and separation of pillars, on the current density was numerically studied to guide the design of μAEs. The normalized height was $Z = z_{pillar}/r_{pillar}$and the normalized separation was $D = r_{domain}/r_{pillar}$. Fig. 2B shows the current density of the μAEs as a function of Z and D. For a given micropillar radius and separation, the higher the normalized height (Z), the larger the current density. For example, for the model with a 100 μm micropillar radius and D of 1.5, the current density of the μAE with 800 μm micropillars is 3.08 times of that of the μAE with 200 μm micropillars. This suggests that the height has a significant impact on the response current for any μAEs. In comparison, a much smaller separation is required to achieve a larger surface area. However, a smaller separation might reduce the current density due to the potential overlap of the diffusion layers. For example, when Z is set to 6, the current density of the μAE with D = 1.05 is 45% of that of the μAE with D = 1.25. Thus, it is reasonable to employ this model to analyze the maximum response current and the current density of the μAE as long as the normalized height and separation are within the above ranges. Such an analysis may benefit the understanding of the performance of μAEs from the geometry point of view.

Characterization of micropillar array electrodes

The SEM images of μAE100, μAE300, μAE500, and a planar electrode (PDMS coated with a gold layer) are shown in Fig. 3(a)–(d). The pillars with the truncated-cone shape were successfully manufactured after repeated soft lithography. The height of micropillars on the cross-sectional images of μAE100, μAE300, and μAE500 (Fig. 3(e)–(g)) was measured as 102.7 ± 1.4 μm, 311.6 ± 2.3 μm, and 515.4 ± 3.2 μm, respectively. The bottom radius of the pillars was approximately 100 μm, while the center-to-center distance of two pillars within the same row or column was around 300 μm. Additionally, there are obvious ripples on the sidewalls of the pillars which were related to the resolution of the layer-to-layer printing. The ripples might be beneficial for raising the surface area to volume ratio of the electrodes. Since the master of μAEs in this study was

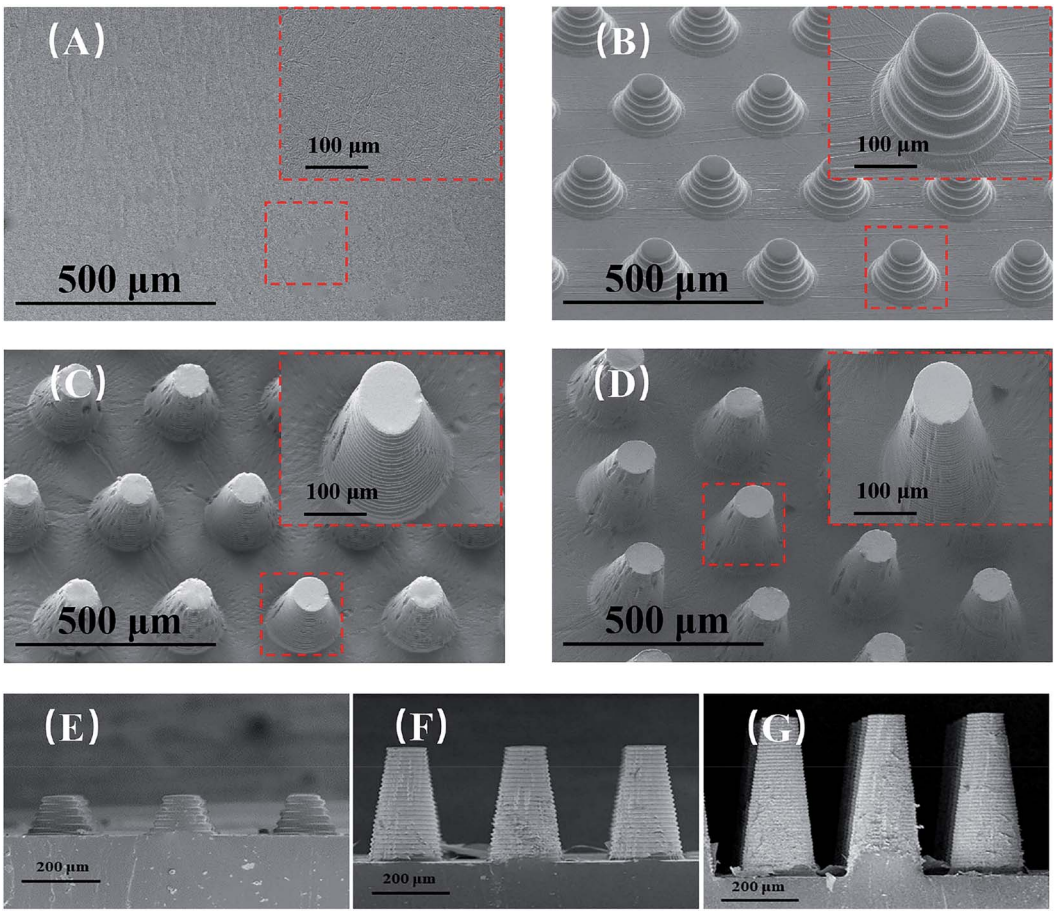

Fig. 3 The SEM images of (A) the planar PDMS electrode, and the PDMS μAEs with (B) 100 μm, (C) 300 μm and (D) 500 μm high pillars. Cross-sectional views of the μAEs with the pillar height of (E) 100 μm, (F) 300 μm and (G) 500 μm.

manufactured by 3D printing, the height of pillars is much higher than those fabricated using MEMS micromachining techniques,[22,23] demonstrating the advantage of the fabrication in this paper.

The cyclic voltammetry (Fig. S4†) was used in a standard redox system of ferrocyanide/ferricyanide with potassium chloride to understand the electrochemical activity of both the planar electrodes and the μAEs with various pillar heights. The CV curves (Fig. 4A) at the scan rate of 100 mV s^{-1} reveals that the absolute value of both the redox and the anodic peak current increase with the increase of the pillar height. The anodic peak current (i_{pa}) obtained from the curves is proportional to the surface area of the electrodes (inset). For example, the i_{pa} and the surface area of μAE500 are approximately 3.3 and 2.13 times higher than those of the planar electrode, respectively. This relationship can be described by a linear model of: i_p (μA) = 26.42 S (mm^2)–56.3 (R^2 = 0.99).

The electroactive area (A, cm^2) was determined using the Randles–Sevcik equation:[36] $i_p = (2.69 \times 10^5)n^{3/2}ACD^{1/2}v^{1/2}$, where i_p is the peak current in amperes, n is the number of electrons involved in the electrochemical reaction, C is the concentration of the analyte in mol cm^{-3}, D is the diffusion coefficient of the species (6.39×10^{-6} cm^2 s^{-1}),[26] and v is the scan rate in V s^{-1}. As shown in Fig. 4B, the electroactive areas of μAE100, μAE300 and μAE500 are 0.67, 1.87 and 3.33 times larger than that of the planar electrode (0.15 ± 0.006 cm^2), respectively. This suggests μAEs effectively increase the electroactive area by incorporating micropillars with different heights. Furthermore, the electroactive area is 67–127% larger than the surface area of each electrode, which might be related to the surface roughness as a result of the 3D printing technique (*e.g.*, stepped structure on the side walls).

The relationship (see Fig. 4C) between the scan rates and the redox peak current of μAEs in 5 mM $K_3[Fe(CN)_6]/K_4[Fe(CN)_6]$ solution was studied in detail to understand the dynamic behavior of the μAEs. The absolute value of both anode (i_{pa}) and cathodic (i_{pc}) peak current is directly proportional to the square root of the scan rates in the range of 0.14 to 0.5. This relationship can be described by $i_{pa} = k\sqrt{v} + b$, where k = 251.45, 278.36, 524.72, and 752.43 for the planar, μAE100, μAE300 and μAE500, respectively. It is obvious that the slope augmented as an increase in the surface area of the electrodes. Moreover, the linear correlation between redox peak current and the square root of the scan rate indicates that the kinetics of μAEs is diffusion-controlled.[36]

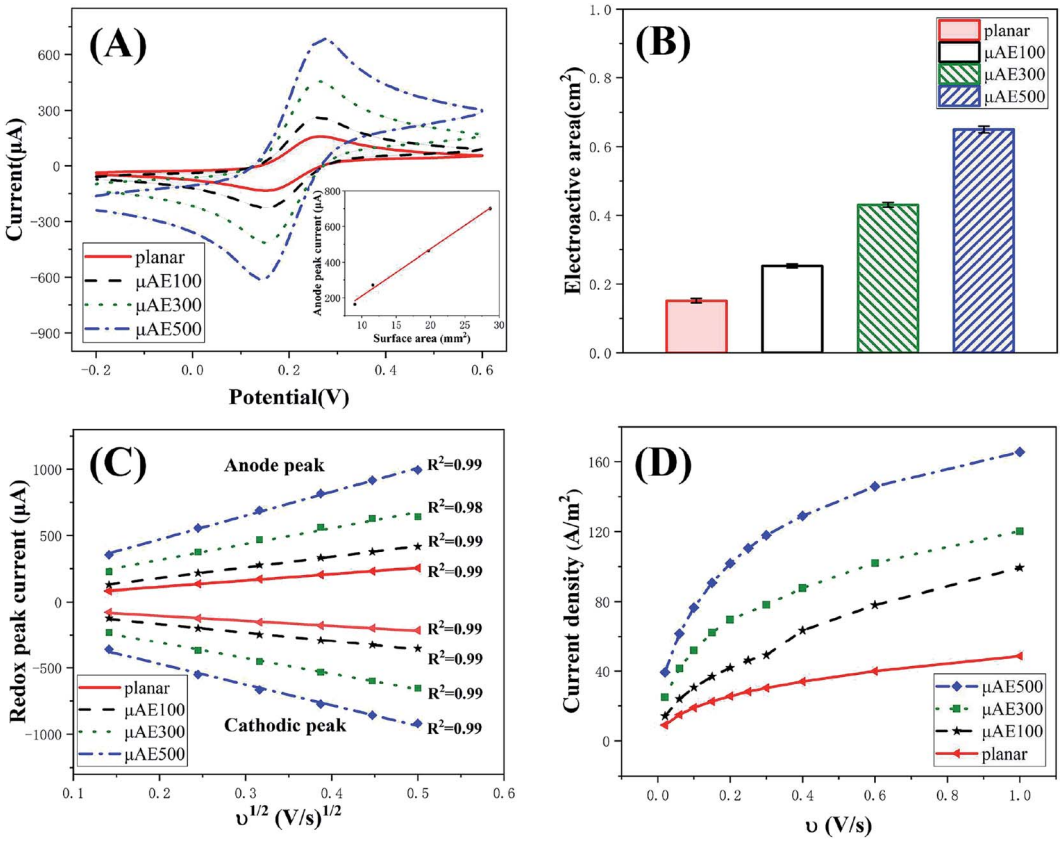

Fig. 4 (A) Cyclic voltammetry of the planar electrode, μAE100, μAE300, and μAE500 in the 5 mM $K_3[Fe(CN)_6]/K_4[Fe(CN)_6]$ solution with 0.5 M KCl. (B) Electroactive area. (C) Anodic and cathodic peak currents as a function of the square root of the scan rates. (D) Variation of current density with scan rate for different electrodes.

The current density of μAEs at distinct scan rates was studied to demonstrate their advantages in improving the detection sensitivity. The relationship between scan rates and the current density is shown in Fig. 4D. The μAEs have higher current densities at any given scan rate in the range of 0.025–1 V s^{-1} (ref. 22) in comparison with the planar electrode. For example, when the scan rate is 20 mV s^{-1}, the current density of the μAE100, μAE300, and μAE500 is 0.56, 1.75 and 3.32 times larger than that of the planar electrode, respectively. According to Prehn *et al.*,[16] when the micropillars are immersed in the diffusion layer, there is no significant difference in the voltammetry between μAEs and the planar electrode at a low scan rate (0.025 V s^{-1}). However, our results reveal that higher micropillars achieve higher current density even at low scan rates. This is because the height of the μAEs is sufficient to allow the penetration through the diffusion layer.

Characterization of Pt–Pd/MWCNTs

The application of Pt–Pd/MWCNTs was explored in modifying the μAEs. Both TEM and XPS techniques were employed to confirm that the current Pt–Pd/MWCNTs had similar morphology and composition to that in the literature, which indicates the successful synthesis of the nanomaterials. The TEM photos (Fig. 5A) of the Pt–Pd/MWCNTs indicates that Pt–Pd nanoparticles were deposited on the surface of MWCNTs without visible aggregation. The mean size of Pt–Pd nanoparticles on the TEM photos was measured to be approximately 4 nm. Additionally, the elementary composition of Pt–Pd/MWCNTs was confirmed by XPS. Fig. 5B clearly shows the signal of Pt 4f and Pd 3d in the samples of the Pt–Pd/MWCNTs, while there are no relevant signals in the acid-treated MWCNTs. The core-level spectra of Pt 4f and Pd 3d (Fig. S5A and B†) indicates that the intensity peaks of Pt $4f_{7/2}$, Pt $4f_{5/2}$, Pd $3d_{5/2}$, and Pd $3d_{3/2}$ appears when the binding energy was 71.9, 75.2, 336.2, and 341.5 eV, respectively. These results reveal the coexistence of Pt (0) and Pd (0) in Pt–Pd/MWCNTs. In addition to introducing larger surface area using micropillars, nanomaterials,[37,38] *e.g.*, Pt nanoparticles (NPs),[39] bismuth NPs,[18] and gold-black,[19] have been widely employed to modify the surface of μAEs to obtain larger response current. However, most nanomaterials are introduced to the surface by electrodeposition, which not only requires precise control of the current and voltage but is limited for the cases of depositing complex nanomaterials or modification of multiple electrodes simultaneously. The current study employed drop cast of complex nanomaterials, Pt–Pd/MWCNTs, to modify the electrode surface. Such materials were recently developed as a novel nanomaterial to modify

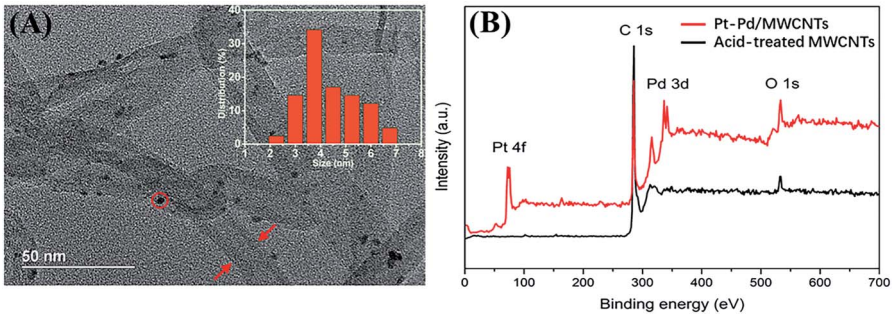

Fig. 5 (A) The TEM photo of Pt–Pd/MWCNTs nanocomposites with the size distribution (inset) of Pt–Pd nanoparticles. (B) The intensity of Pt–Pd/MWCNTs nanocomposites from XPS wide scan.

the glassy carbon electrode for the sensitive detection of hydrogen peroxide.[40] This strategy combines the excellent catalytic ability of platinum–palladium alloy nanoparticles with the outstanding conductivity of carbon nanotubes, enabling a higher detection sensitivity of the sensor.

Detection of hydrogen peroxide

Many biomarkers such as glucose, sarcosine, and cholesterol can be oxidized to produce H_2O_2 which can be quantitatively measured using either electrochemical[10] or colorimetric techniques.[41] The μAE500 modified with Nafion/Pt–Pd/MWCNTs nanocomposites were characterized by assessing their ability in detecting H_2O_2 to evaluate the influence of nanocomposite modification on the sensitivity of the detection.

The CV curves of the μAE500-Nafion/Pt–Pd/MWCNTs are shown in Fig. 6A at different H_2O_2 concentrations. The CV curves of the μAE500-Nafion/Pt–Pd/MWCNTs are shown in Fig. 6A at different H_2O_2 concentrations. The μAE500 was modified by 1 μL 2 mg mL^{-1} Pt–Pd/MWCNTs nanocomposites. The onset oxidation potential for H_2O_2 was about +0.4 V. The oxidation current became maximum at the potential of approximately +0.6 V and maintained an almost constant value when the potential was up to +0.8 V. Therefore, the potential of +0.6 V was chosen as the applied potential in all following experiments. In the absence of H_2O_2, the oxidation current was as low as 11.5 μA (the red solid line). As the concentration of H_2O_2 was increased to 500 μM and 1500 μM, the oxidation current increased to about 18.3 μA and 21.7 μA, respectively. This clearly demonstrated the good oxidation ability of the modified electrodes for hydrogen peroxide.

The effect of nanocomposites modification for different electrodes was studied by evaluating the oxidation current in the 100 μM H_2O_2 solution (Fig. 6B). Regardless of the modification, the oxidation current increased with the increase of the electrode surface area. The oxidation current of modified electrodes was approximately 1.32–2.24 times higher than the same electrode without modification. For example, the response current (629.7 ± 24.9 nA) of the modified μAE500 was 2.33 times as big as that (270.5 ± 10.9 nA) of the μAE500. Further, the output current of the modified μAE500 was approximately 8 times that of the planar electrode without modification. Therefore, it can be concluded that both larger surface area enabled by high pillars and the nanocomposite modification contributed to the larger oxidation current.

The influence of the nanocomposite amount (1–8 mg mL^{-1}) on detection sensitivity was studied to optimize the electrochemical detection capability of the μAE500. Fig. S6† depicts the chronoamperometric curves of μAE500-Nafion/Pt–Pd/MWCNTs and planar electrodes with Nafion/Pt–Pd/MWCNTs in H_2O_2 solutions with various concentrations (0–100 μM). A good linear relationship between the current and the H_2O_2 concentration was found for all electrodes, regardless of the modification conditions. The slopes of the linear models indicated that the

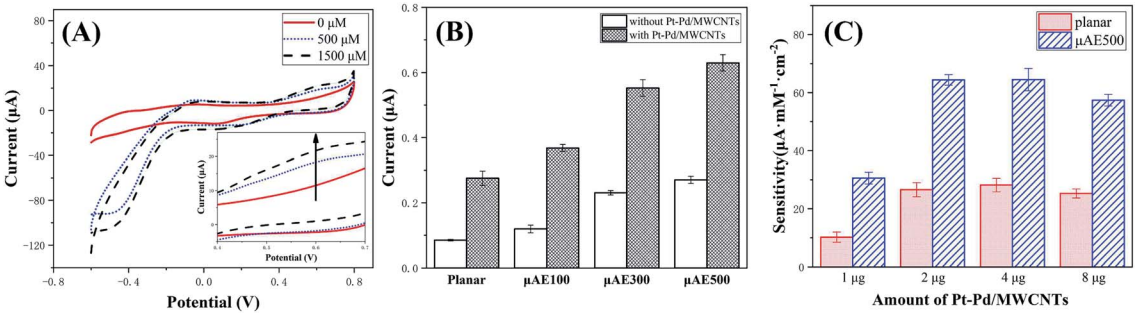

Fig. 6 (A) CV curves of the Nafion/Pt–Pd/MWCNTs/μAE500 electrode in 0, 500, and 1500 μM H_2O_2 solutions. (B) Oxidation currents of various electrodes with and without modification using Pt–Pd/MWCNTs. (C) Comparison of sensitivity between the planar and μAE500 electrodes coated with 1, 2, 4, or 8 μg Pt–Pd/MWCNTs.

response current of the modified electrodes dramatically increased with the increase of concentration of the nanomaterials (in other words, the quantity of nanocomposites coated on the electrodes).

Fig. 6C shows the sensitivity of both the planar and the μAE500. Both the planar and the μAE500 electrodes showed increased sensitivity when the amount of Pt–Pd/MWCNTs coated on the electrodes was increased from 1 μg to 4 μg. The increase was more pronounced at 1 and 2 μg and reached a peak at 4 μg. It leveled off from 4 μg. At the peak, the sensitivity of the μAE500 is 2.3 times that of the planar electrode. The level-off is related to the agglomeration of the nanomaterial in the small area of the electrode. After agglomeration, the electron transfer process was suppressed due to the reduced contact area,[42] leading to a reduction in the sensitivity. The higher sensitivity of the modified μAE500 is due to the larger surface area of the μAE500, which prevents the agglomeration of the nanomaterial. Additionally, the nanomaterials immobilized on both the top and sidewalls of each pillar probably extend far beyond the diffusion layer of the planar electrode, leading to more and efficient contact with analyzes.

Compared to the conventional method of electrodepositing nanomaterials on the surface of μAEs,[18,19] the drop-cast method to deposit nanomaterials on electrodes was straightforward and flexible. Moreover, the modified μAE500 offered comparable sensitivity (64.5 μA mM^{-1} cm^{-2}) in detecting hydrogen peroxide, compared with the planar electrode modified by the electrodeposition of Ag NPs/GCE[43] (32.9 μA mM^{-1} cm^{-2}), NiHCNFe/ppy/GCE[44] (88.33 μA mM^{-1} cm^{-2}), and Pd NWs/NTs[45] (173–363 μA mM^{-1} cm^{-2}). These results imply that the μAEs with high micropillars and a large surface area modified by drop-casting nanomaterial have great potential in the development of sensitive and cost-effective electrochemical sensors.

Detection of sarcosine

The μAE500 modified with Pt–Pd/MWCNTs were employed to detect sarcosine using chronoamperometric (CA) measurement to demonstrate the sensitivity and reliability of the μAEs. The CA measurement was set at a constant potential of 0.6 V (*versus* the reference electrode of AgCl) and the pulse width of 90 s. As shown in Fig. 7, the absolute value of response current increased proportionally with the increase of sarcosine concentration. The current–concentration curve of sarcosine derived from CA measurements is shown in the inset of Fig. 7. The relationship between current (I) and the sarcosine concentration (C) can be described by a linear model I (μA) = 0.00154 C (μM) + 0.0978 (R^2 = 0.99) when the concentration is in the range of 5–60 μM. The sensitivity was calculated by dividing the slope of the above linear model by the projected area of the electrode. The sensitivity is found to be 17.1 μA mM^{-1} cm^{-2} with a LOD (S/N = 3) of 1.28 μM.

The detection performance of various biosensors for sarcosine is listed in Table S3.† Although different sensors have significantly distinct linear detection ranges and LODs, the μAE in this study has a larger linear range (5–60) but a lower LOD in comparison to the glassy carbon electrodes modified by Pt@ZIF8.[46] Since the current response of μAEs increased with its pillar height/surface area, the μAEs with much higher pillars/surface area will dramatically reduce the LOD.

The sarcosine concentration may vary either from 0 to 5 or from 5 to 60 in different tissues of the healthy and prostate cancer patient, respectively.[47] The concentration of sarcosine higher than 2.67 μM maybe a clear indication of prostate cancer.[48] The LOD (1.28 μM) of μAE500 for sarcosine detection is much smaller than the cutoff value of μM. Therefore, the μAE500 in this paper demonstrates its potential in detecting sarcosine from either serum or urine for clinical applications with high sensitivity and reliability.

Conclusions

This paper reports the facile fabrication, surface modification, and characterization of a PDMS-based micropillar electrode array coated with gold films. The repeated soft lithography of the 3D printed master was employed to manufacture μAEs to dramatically reduce the fabrication cost. Numerical study and experiments showed that the current density of μAEs was proportional to their surface area. Even at a low scan rate, μAEs acquired a much larger current density than the planar electrode. This is favorable for electrochemical detection of low

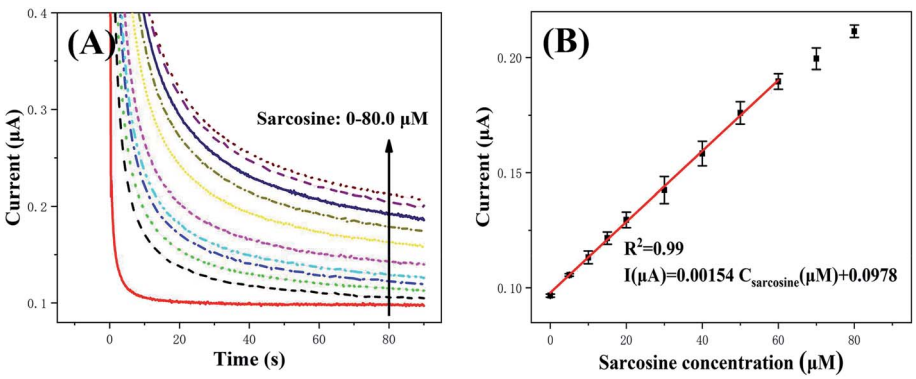

Fig. 7 (A) Chronoamperometric curves of Nafion/SO_x/Pt–Pd/MWCNTs/μAE500 electrode when the concentration of sarcosine was increased from 0 to 80.0 μM (from bottom to top). (B) Current response at different sarcosine concentrations.

abundance analytes. Moreover, μAEs were coated using home-made platinum–palladium/multi-walled carbon nanotubes (Pt–Pd/MWCNTs) to further enhance detection sensitivity. Hydrogen peroxide and sarcosine were detected to demonstrate the electrochemical performance of Nafion/Pt–Pd/MWCNTs/μAEs. As a result of the larger surface of μAEs and the excellent electrocatalytic performance of the nanocomposite, the output current of the modified μAE500 was approximately 8 times greater than that of the planar electrode without modification. The sensitivity of the Nafion/Pt–Pd/MWCNTs/μAE500 was 1.5 times higher than that of the planar electrode modified at the same condition. The linear detection range, sensitivity and LOD (S/N = 3) of the sarcosine biosensors (μAE500) was 5–60 μM, 17.1 μA mM^{-1} cm^{-2} and 1.28 μM, respectively. The outcome of this study is significant for the design and application of the μAEs in electrochemical detection of biomarkers.

Conflicts of interest

There are no conflicts to declare.

Acknowledgements

This work was supported by the National Natural Science Foundation of China (Grant No. 11772112) and Shenzhen Science and Technology Innovation Committee (Grant No. JCYJ20170413105329648).

References

1 E. Stern, *et al.*, Label-free biomarker detection from whole blood, *Nat. Nanotechnol.*, 2010, **5**(2), 138–142.
2 J. Wu, *et al.*, Biochemical analysis on microfluidic chips, *TrAC, Trends Anal. Chem.*, 2016, **80**, 213–231.
3 X. Huang, Smartphone-based analytical biosensors, *Analyst*, 2018, **143**(22), 5339–5351.
4 C. Li, *et al.*, Improvement of enzyme-linked immunosorbent assay for the multicolor detection of biomarkers, *Chem. Sci.*, 2016, **7**(5), 3011–3016.
5 B. V. Chikkaveeraiah, *et al.*, Electrochemical immunosensors for detection of cancer protein biomarkers, *ACS Nano*, 2012, **6**(8), 6546–6561.
6 M. M.-C. Cheng, *et al.*, Nanotechnologies for biomolecular detection and medical diagnostics, *Curr. Opin. Chem. Biol.*, 2006, **10**(1), 11–19.
7 S. A. Zaidi, *et al.*, Progress in cancer biomarkers monitoring strategies using graphene modified support materials, *Talanta*, 2020, 210.
8 T. Hong, *et al.*, Recent advances in the fabrication and application of nanomaterial-based enzymatic microsystems in chemical and biological sciences, *Anal. Chim. Acta*, 2019, **1067**, 31–47.
9 J. Guo and X. Ma, Simultaneous monitoring of glucose and uric acid on a single test strip with dual channels, *Biosens. Bioelectron.*, 2017, **94**, 415–419.
10 Q. Wang, *et al.*, Amperometric sarcosine biosensor with strong anti-interference capabilities based on mesoporous organic-inorganic hybrid materials, *Biosens. Bioelectron.*, 2019, **141**, 111431.
11 N. Agnihotri, *et al.*, Non-enzymatic electrochemical detection of cholesterol using β-cyclodextrin functionalized graphene, *Biosens. Bioelectron.*, 2015, **63**, 212–217.
12 G. Liu, *et al.*, A carbon nanotube-based high-sensitivity electrochemical immunosensor for rapid and portable detection of clenbuterol, *Biosens. Bioelectron.*, 2011, **28**(1), 308–313.
13 G.-h. Wu, *et al.*, Non-enzymatic electrochemical glucose sensor based on platinum nanoflowers supported on graphene oxide, *Talanta*, 2013, **105**, 379–385.
14 J. Guo, Uric Acid Monitoring with a Smartphone as the Electrochemical Analyzer, *Anal. Chem.*, 2016, **88**(24), 11986–11989.
15 Y. Tan, *et al.*, Dual-channel Microchip Electrophoresis with Amperometric Detection System for Rapid Analysis of Cefoperazone and Sulbactam, *Anal. Sci.*, 2019, **35**(10), 1103–1109.
16 G. Zhu, *et al.*, A gold nanoparticle-modified indium tin oxide microelectrode for in-channel amperometric detection in dual-channel microchip electrophoresis, *Anal. Methods*, 2017, **9**(29), 4319–4326.
17 F. Liu, *et al.*, Three-dimensional graphene micropillar based electrochemical sensor for phenol detection, *Biosens. Bioelectron.*, 2013, **50**, 387–392.
18 X. Hu, *et al.*, Miniaturized electrochemical sensor with micropillar array working electrode for trace lead online measurement in tap water, *J. Micromech. Microeng.*, 2019, **29**(10), 5000–5005.
19 S. Numthuam, *et al.*, Synergistic effects of micro/nano modifications on electrodes for microfluidic electrochemical ELISA, *Sens. Actuators, B*, 2011, **156**(2), 637–644.
20 Q. Liu, *et al.*, Simultaneous detection of trace Ag(I) and Cu(II) ions using homoepitaxially grown GaN micropillar electrode, *Anal. Chim. Acta*, 2020, **1100**, 22–30.
21 Y. Song and C. Wang, High-power biofuel cells based on three-dimensional reduced graphene oxide/carbon nanotube micro-arrays, *Microsyst. Nanoeng.*, 2019, **5**, 46.
22 R. Prehn, A. Llibertat, D. Sánchez-Molas, M. Duch, N. Sabaté, J. del Campo, F. Xavier Muñoz and R. G. Compton, Microfabrication and characterization of cylinder micropillar array electrodes, *J. Electroanal. Chem.*, 2011, 361–370.
23 D. Sanchez-Molas, *et al.*, High Aspect-Ratio, Fully Conducting Gold Micropillar Array Electrodes: Silicon Micromachining and Electrochemical Characterization, *J. Phys. Chem. C*, 2012, **116**(35), 18831–18846.
24 E. J. F. Dickinson, *et al.*, Theory of chronoamperometry at cylindrical microelectrodes and their arrays, *J. Phys. Chem. C*, 2008, **112**(31), 11637–11644.
25 N. C. de Moraes, *et al.*, Design of novel, simple, and inexpensive 3D printing-based miniaturized electrochemical platform containing embedded disposable detector for analytical applications, *Electrophoresis*, 2019, 278–286.
26 E. C. Zoski, *Handbook of electrochemistry*, 2007.

27 Z. Chen, *et al.*, Cell elasticity measurement using a microfluidic device with real-time pressure feedback, *Lab Chip*, 2020, **20**(13), 2343–2353.
28 C. Chen, *et al.*, Dynamic screening and printing of single cells using a microfluidic chip with dual microvalves, *Lab Chip*, 2020, **20**(7), 1227–1237.
29 Q. Chen, *et al.*, Controlled assembly of heterotypic cells in a core-shell scaffold: organ in a droplet, *Lab Chip*, 2016, **16**(8), 1346–1349.
30 W. Liu and J.-M. Lin, Online Monitoring of Lactate Efflux by Multi-Channel Microfluidic Chip-Mass Spectrometry for Rapid Drug Evaluation, *ACS Sensors*, 2016, **1**(4), 344–347.
31 B. Osmani, *et al.*, Morphology and conductivity of Au films on polydimethylsiloxane using (3-mercaptopropyl)trimethoxysilane (MPTMS) as an adhesion promoter, in *Electroactive Polymer Actuators and Devices*, EAPAD, 2016, 2016.
32 H. Chen, *et al.*, Multiplexed detection of cancer biomarkers using a microfluidic platform integrating single bead trapping and acoustic mixing techniques, *Nanoscale*, 2018, **10**(43), 20196–20206.
33 H. Chen, *et al.*, High-throughput, deterministic single cell trapping and long-term clonal cell culture in microfluidic devices, *Lab Chip*, 2014, **15**(4), 1072–1083.
34 H. Y. Chen, *et al.*, Cardiac-like flow generator for long-term imaging of endothelial cell responses to circulatory pulsatile flow at microscale, *Lab Chip*, 2013, **13**(15), 2999–3007.
35 X. Zhu, *et al.*, Immobilization of superoxide dismutase on Pt–Pd/MWCNTs hybrid modified electrode surface for superoxide anion detection, *Biosens. Bioelectron.*, 2015, **67**, 79–85.
36 D. M. R. D. Rooij, *Electrochemical Methods: Fundamentals and Applications*, 2004, **50**(5), 137–360.
37 C. Li, *et al.*, Recent Progress in Stimulus-Responsive Two-Dimensional Metal–Organic Frameworks, *ACS Mater. Lett.*, 2020, **2**(7), 779–797.
38 C. Li, *et al.*, Ferrocene-based metal-organic framework as a promising cathode in lithium-ion battery, *Chem. Eng. J.*, 2021, 404.
39 J. Gao, *et al.*, Simultaneous detection of glucose, uric acid and cholesterol using flexible microneedle electrode array-based biosensor and multi-channel portable electrochemical analyzer, *Sens. Actuators, B*, 2019, **287**, 102–110.
40 K. J. Chen, *et al.*, Bimetallic PtM (M=Pd, Ir) nanoparticle decorated multi-walled carbon nanotube enzyme-free, mediator-less amperometric sensor for H(2)O(2), *Biosens. Bioelectron.*, 2012, **33**(1), 120–127.
41 C. Chen, *et al.*, Novel wax valves to improve distance-based analyte detection in paper microfluidics, *Anal. Chem.*, 2019, **91**(8), 5169–5175.
42 A. Krittayavathananon, *et al.*, Comparing the effect of different surfactants on the aggregation and electrical contact properties of graphene nanoplatelets, *Applied Materials Today*, 2018, **12**, 163–167.
43 E. Kurowska, *et al.*, Silver nanowire array sensor for sensitive and rapid detection of H2O2, *Electrochim. Acta*, 2013, **104**, 439–447.
44 P. A. Fiorito and S. I. C. de Torresi, Hybrid nickel hexacyanoferrate/polypyrrole composite as mediator for hydrogen peroxide detection and its application in oxidase-based biosensors, *J. Electroanal. Chem.*, 2005, **581**(1), 31–37.
45 B. Patella, *et al.*, A nanostructured sensor of hydrogen peroxide, *Sens. Actuators, B*, 2017, **245**, 44–54.
46 H. Yang, *et al.*, Nano Pt@ ZIF8 modified electrode and its application to detect sarcosine, *J. Electrochem. Soc.*, 2018, **165**(5), H247–H250.
47 A. Sreekumar, *et al.*, Metabolomic profiles delineate potential role for sarcosine in prostate cancer progression, *Nature*, 2009, **457**, 910.
48 A. Roy, *et al.*, Sarcosine Prostate Cancer Biomarker Detection by Controlling Oxygen in NiO_x Membrane on Vertical Silicon Nanowires in Electrolyte-Insulator-Nanowire Structure, *Anal. Chem.*, 2020, **92**(12), 8064–8071.